Mon. Not. R. Astron. Soc. **312**, 817–826 (2000)

Effects of Kerr space–time on spectral features from X-ray illuminated accretion discs

A. Martocchia,[1★] V. Karas[2★] and G. Matt[3★]

[1]*SISSA-ISAS, Via Beirut 2/4, I-34014 Trieste, Italy*
[2]*Astronomical Institute, Charles University Prague, V Holešovičkách 2, CZ-180 00 Praha, Czech Republic*
[3]*Dipartimento di Fisica, Università degli Studi 'Roma Tre', Via della Vasca Navale 84, I-00146 Roma, Italy*

Accepted 1999 October 15. Received 1999 October 15; in original form 1999 June 21

ABSTRACT

We performed detailed calculations of the relativistic effects acting on both the reflection continuum and the iron line from accretion discs around rotating black holes. Fully relativistic transfer of both illuminating and reprocessed photons has been considered in Kerr space–time. We calculated overall spectra, line profiles and integral quantities, and present their dependences on the black hole angular momentum. We show that the observed EW of the lines is substantially enlarged when the black hole rotates rapidly and/or the source of illumination is near above the hole. Therefore, such calculations provide a way to distinguish between different models of the central source.

Key words: accretion, accretion discs – black hole physics – line: formation – relativity – galaxies: active – X-rays: galaxies.

1 INTRODUCTION

Radiation emitted in the X-ray band by active galactic nuclei (AGN) and Galactic black hole candidates (BHCs) exhibits the imprints of strong gravitational fields and orbital rapid motion of matter near a black hole. Here we adopt the model with a rotating back hole surrounded by an accretion disc.

The very first studies of light propagation in the Kerr metric were performed in the 1970s (Bardeen, Press & Teukolsky 1972; Cunningham & Bardeen 1973; Cunningham 1975), and it was argued that the observed radiation should be substantially affected by the presence of a black hole and by its rotation. In the last few years, even before the great excitement aroused by the *ASCA* detection of the relativistic iron Kα line in the spectrum of the Seyfert 1 galaxy MCG-6-30-15 (Tanaka et al. 1995), many authors modelled the effects of special and general relativity on the line profiles under various physical and geometrical assumptions (e.g. Fabian et al. 1989). Calculations of line profiles from a disc-like source in Kerr space–time have been performed by Laor (1991), Kojima (1991), Hameury, Marck & Pelat (1994), Karas, Lanza & Vokrouhlický (1995), Bromley, Chen & Miller (1997), Fanton et al. (1997), Dabrowski et al. (1997), Čadež, Fanton & Calvani (1998) and others. Nowadays, these studies are particularly relevant for the understanding of AGN in view of the above mentioned detection of line profiles, which suggests substantial relativistic effects in many objects (Nandra et al. 1997).

★ E-mail: martok@sissa.it (AM); vladimir.karas@mff.cuni.cz (VK); matt@haendel.fis.uniroma3.it (GM)

Various simplifying assumptions have been adopted in previous calculations. Often line profiles have been calculated independently of the underlying reflection continuum (Guilbert & Rees 1988; Lightman & White 1988), which is however produced along with the line after illumination of the disc by some primary X-ray source. Even when considered, calculations of light propagation were performed in the Schwarzschild metric. Matt, Perola & Piro (1991) adopted a weak-field approximation. Recently, Maciołek-Niedźwiecki & Magdziarz (1988) and Bao, Wiita & Hadrava (1998) made use of fully relativistic codes, but still in the Schwarzschild metric. Morever, a simple power-law parametrization of the disc emissivity usually has been adopted, e.g. the one which follows from the Page & Thorne (1974) model, while the actual emissivity is substantially more complex and depends on the geometry of the illuminating matter (Matt et al. 1991; Martocchia & Matt 1996).

Self-consistent calculations of iron lines and continuum together are still missing in the case of the Kerr metric. This problem is thus examined in the present paper. Reflected light rays are properly treated as geodesics in the curved space–time and, furthermore, light propagation from the primary, illuminating source to the reflecting material is also calculated in a fully relativistic approach. The adopted point-like geometry for the primary X-ray emitting region (Section 2.1) is clearly a simplification, but can be considered as a rough phenomenological approximation to more realistic models. Off-axis flares, which would be expected from magnetic reconnection above the accretion disc, have been considered by Yu & Lu (2000) and Reynolds et al. (1999) in the Schwarzschild and the Kerr metric,

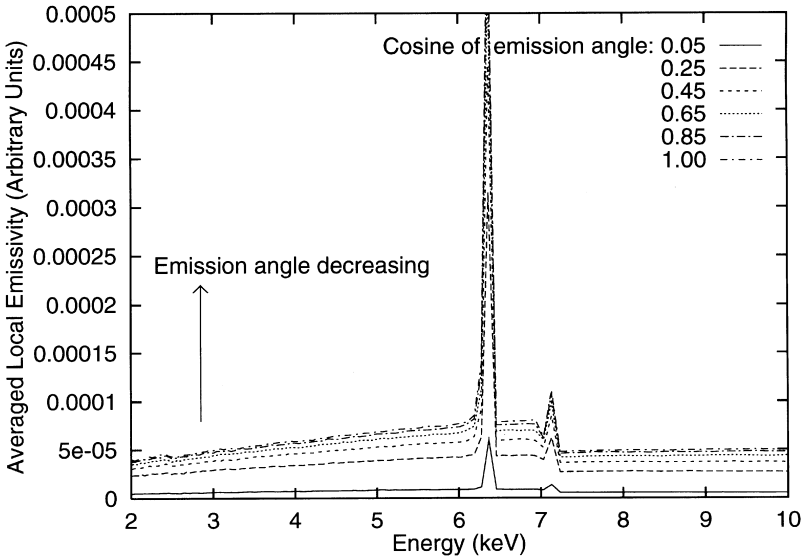

Figure 1. Examples of local spectra $F(E)$ around the iron line rest energy, $E_0 = 6.4\,\mathrm{keV}$. Only angular dependences of the outgoing flux are shown here: F represents the radiation flux averaged over the incident angle of the photons from the primary source.

respectively. More complex scenarios, like hot coronae and non-Keplerian accretion flows, would be very interesting to explore but are beyond the scope of this paper.

2 AN ILLUMINATED DISC IN THE KERR METRIC

2.1 The model

We adopt the model described by Martocchia & Matt (1996): a geometrically thin equatorial disc of cold (neutral) matter, illuminated by a stationary point-like source on the symmetry axis at height h. The local emissivity of the disc has been computed following Matt et al. (1991), taking into account the energy and impinging angle of illuminating photons, as seen by the rotating matter in the disc. Then the transfer of photons leaving the disc was carried out according to Karas, Vokrouhlický & Polnarev (1992).

A similar model of illumination has been used by Henry & Petrucci (1997), who call it an *anisotropic illumination model*, and by other authors (Reynolds et al. 1999, and references cited therein). Bao et al. (1998) used a fixed direction of impinging photons (as if the source were distant, possibly displaced from the rotation axis); however, these authors did not solve the radiation transfer within the disc. This is an important point, as different values of h correspond to substantially different illumination of the disc in the local frame corotating with the matter, and consequently to different emissivity laws, $I(r, h)$. With decreasing h, the effect of light bending is enhanced and the fraction of X-ray photons impinging onto the disc is increased with respect to those escaping to infinity and contributing to the direct (primary) continuum component. Moreover, photons arriving to the disc at radii $\lesssim 13h$ are blueshifted, so that the fraction of photons with energies above the photoionization threshold is increased.

It has been argued (e.g. Martocchia & Matt 1996) that a way to discriminate between static and spinning black holes could be based on the fact that the innermost stable orbit $r_{\rm ms}(a, m)$ of a fast-rotating black hole lies close to the event horizon and approaches the gravitational radius $r_{\rm g}(a, m) \to m$ for a maximally rotating Kerr hole with the limiting value of $a \to m$ (we use standard notation, Boyer–Lindquist coordinates[1] and geometrized units $c = G = 1$; e.g. Chandrasekhar 1983).

Highly redshifted features would then represent an imprint of photons emitted at extremely small disc radii, which is possible only near fast-rotating black holes. Other explanations are also viable but require more complicated models of the source (compared to purely Keplerian, geometrically thin discs). Reynolds & Begelman (1997) pointed out that the difference between spectra of rapidly versus slowly rotating black holes would be much smaller if efficient line emission is allowed also from free-falling matter inside the last stable orbit, and they applied this assumption to the reddish line profile observed during a low-flux state of MCG–6-30-15 (Iwasawa et al. 1996). If this is the case, the presence of an extended red tail of the line could no longer be used as evidence for rapid rotation of the black hole, whereas validity of the 'spin paradigm' (the often made suggestion that rotating black holes are associated with jet production and radio loudness) remains preserved. The problem can be solved by calculating in detail the optical thickness and the ionization state of the free-falling matter, as in Young, Ross & Fabian (1998), who noted that the reflection component in MCG–6-30-15 is not consistent with the expected ionization state of the matter inside $r_{\rm ms}$.

2.2 The emissivity laws

We used a Monte Carlo code to calculate photon transfer within the disc (Matt et al. 1991). The resulting local spectra in the frame comoving with the disc matter are shown in Fig. 1. Assumptions about local emissivity, disc shape and rotation law can be varied in

[1] We recall that the Boyer–Lindquist radial coordinate is directly related to the circumference of $r =$ const circles in the equatorial plane. Coordinate separation between $r_{\rm ms}(a, m)$ and $r_{\rm g}$ obviously decreases when $a \to m$, but proper radial distance (which has direct physical meaning) between these two circles increases as $(m - a)^{-1/6}$. What is however essential for our discussion of observed radiation fluxes are local emissivities and the total outgoing flux, which is obtained by summing over individual contributions of $r =$ const rings. When expressed in terms of r, as we see in Fig. 2, the local emissivity is large near the inner edge and becomes very anisotropic when a approaches its limiting value for the maximally rotating hole.

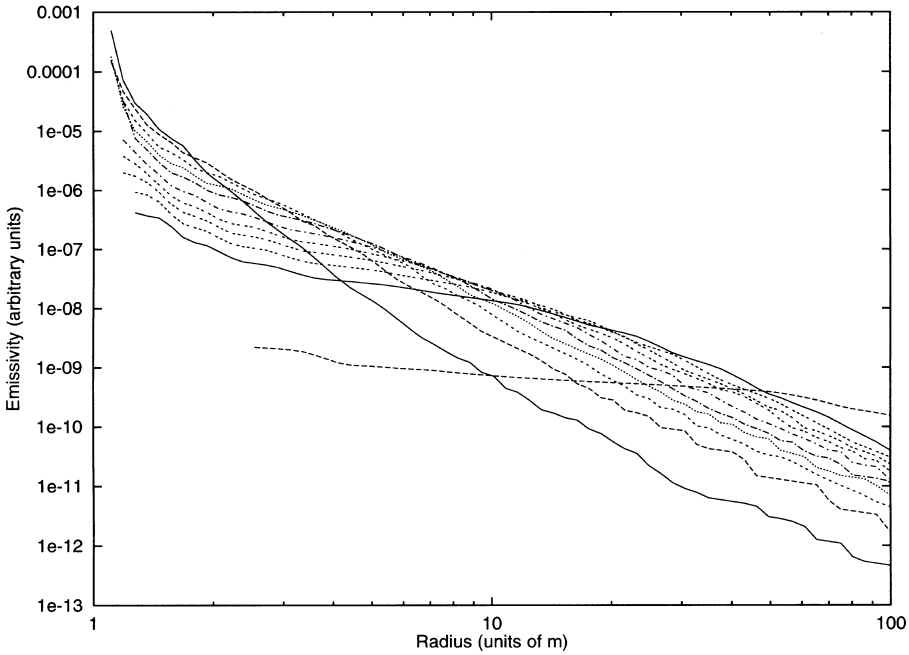

Figure 2. Emissivity laws $I(r)$ (in arbitrary units) corresponding to different source heights above an extreme Kerr hole, as discussed in Martocchia & Matt (1997). Looking at the right side of the diagram the curves correspond, from top to bottom, to heights of 100, 20, 15, 12, 10, 8, 6, 5, 4, 3 and 2 (units of m). The curves steepen when h decreases, which corresponds to increasing anisotropy of emission.

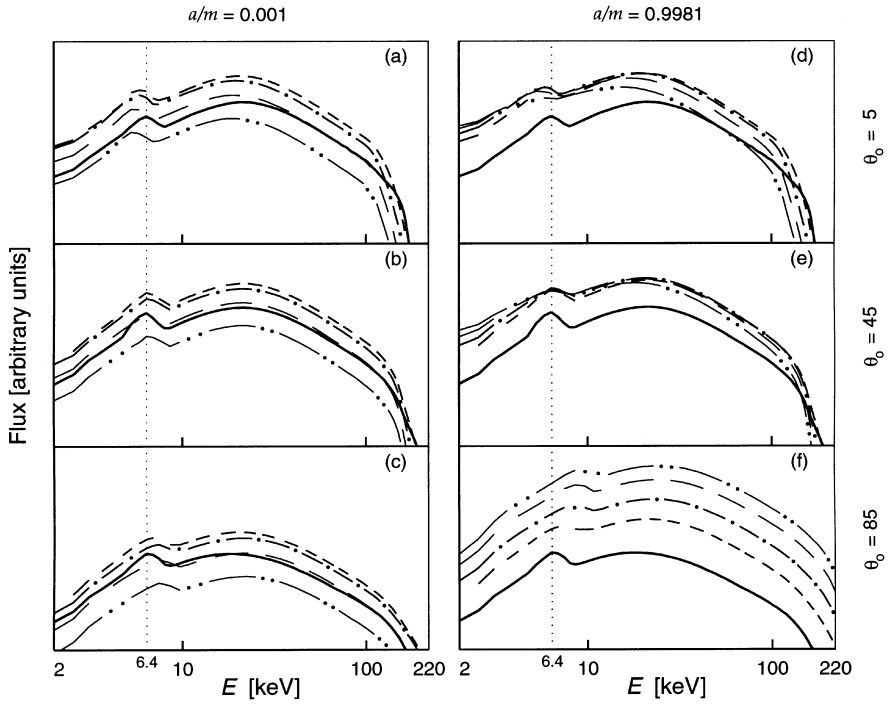

Figure 3. Examples of broad-band (2–220 keV) spectra for three inclination angles ($\theta_o = 5°$, 45° and 85°). The following types of lines have been used in this graph to indicate the source height (in Boyer–Lindquist coordinates): $h = 100\,m$ – thick solid line; $h = 20\,m$ – short-dashed; $h = 10\,m$ – dot-dashed; $h = 6\,m$ – long-dashed; $h = 4\,m$ – double-dot-dashed. The left panel corresponds to a slowly rotating black hole, while the right panel shows the case of rapid rotation, as indicated on the top. Here we considered a disc extending down to the innermost stable orbit. The outer edge is at $r_{out} = 100\,m$.

our code in order to account for different accretion models, but here we describe only the case of standard Keplerian, geometrically thin and optically thick discs for simplicity. Let us note that any radial inflow decreases the observed line widths when compared with the corresponding case of a Keplerian disc. While in other works the disc emissivity often has been described as a power law ($\propto r^{-s}$), we made use of the emissivities derived by Martocchia & Matt (1997) through integration of geodesics from the primary source (Fig. 2). The source distance h stays here, instead of the power-law index s, as one of the model parameters.

2.3 Spectral features

Illumination of cold matter in the disc by the primary, hard X-ray flux results in a Compton-reflection component with specific signatures of bound-free absorption and fluorescence. The most prominent iron features are gathered in a narrow energy range: Kα and Kβ lines with rest energies at 6.4 keV and 7.07 keV, respectively, and the iron edge at 7.1 keV. On the other hand, the overall continuum is rather broad and it is best illustrated in the energy range $E = 2$–220 keV (Figs 3 and 4). The continuum gets broader with increasing inclination owing to Doppler shifts. The large spread in blueshifts and redshifts blurs the photoelectric

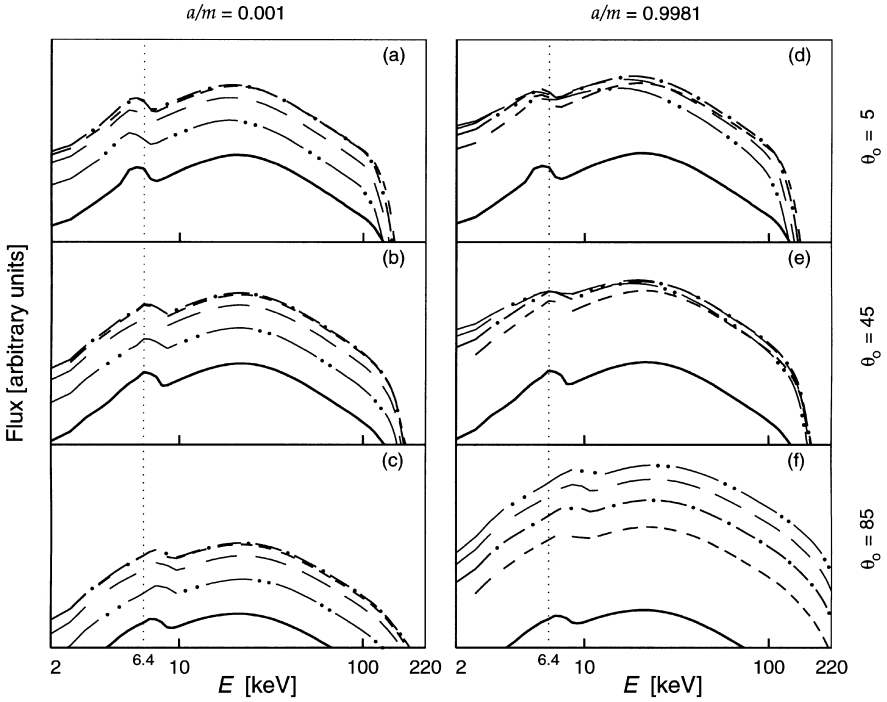

Figure 4. As in the previous figure, but for $r_{\rm out} = 34\,m$.

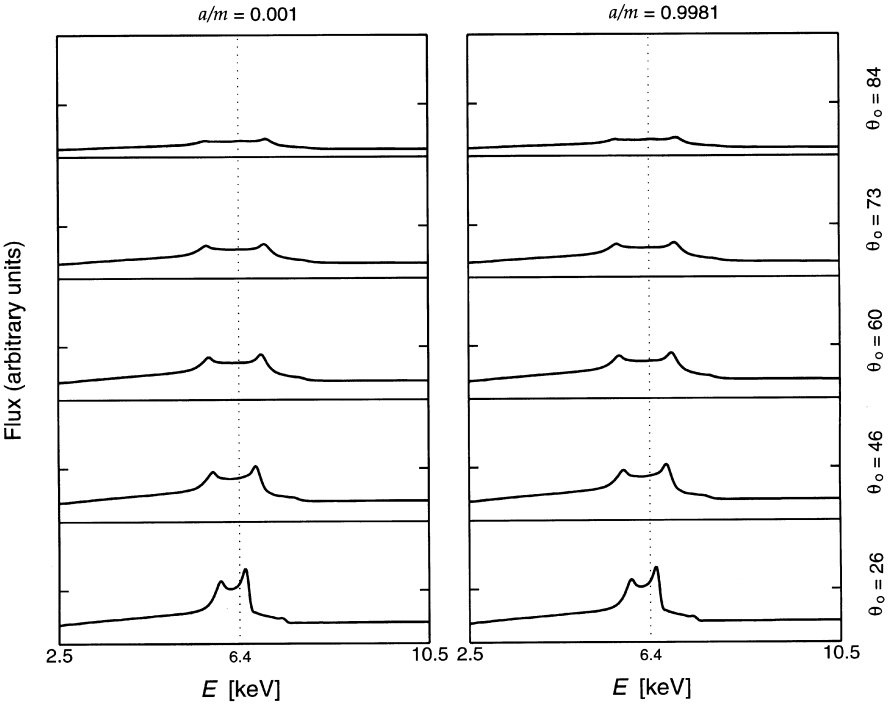

Figure 5. Narrow-band (2.5–10.5 keV) spectra. Calculations have been performed for both non-rotating (left) and maximally rotating (right) holes. The emitting area is comprised of the innermost stable orbit ($r_{\rm in} = r_{\rm ms} = 6\,m$ and $1.23\,m$, respectively) and $r_{\rm out} = 100\,m$. Inclination angles are (from top to bottom): $\cos\theta_{\rm o} = 0.1$, 0.3, 0.5, 0.7 and 0.9. $h = 100\,m$. The vertical axis has a logarithmic scale.

edge at 7.1 keV and results in broad troughs. This can be seen better after increasing the energy resolution, i.e. in the narrow band spectra (next section). The overall spectrum is also sensitive to inclination angles, being more intense when seen pole-on ($\theta_o = 0$).

Line profiles in real spectra must result from a subtraction of the proper underlying continuum, taking into account the relativistic smearing of the iron edge. This work has been already started by several authors in the Schwarzschild metric (Życki, Done & Smith 1997, 1998; Maciołek-Niedźwiecki & Magdziarz 1998; Young et al. 1998) and developed further here, in the case of sources around rotating black holes. The effects of inclination on the smearing and smoothing of all spectral features may be dramatic in the Kerr metric not only because of substantial energy shifts of photons emitted at the innermost radii, but also as a result of the mutual combination of this effect on both the iron line and

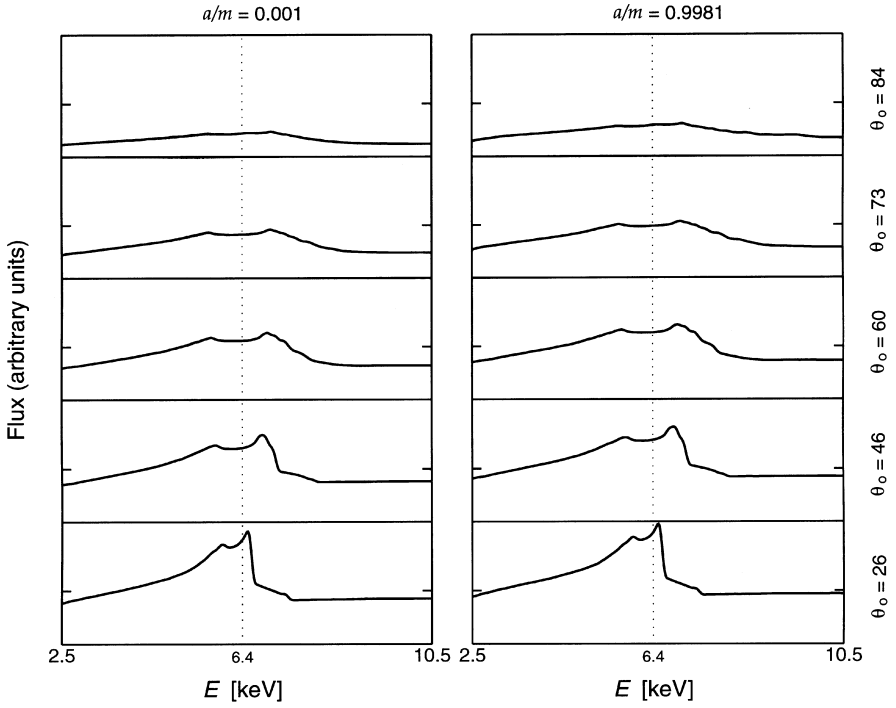

Figure 6. As in previous figure but for $h = 20\,m$.

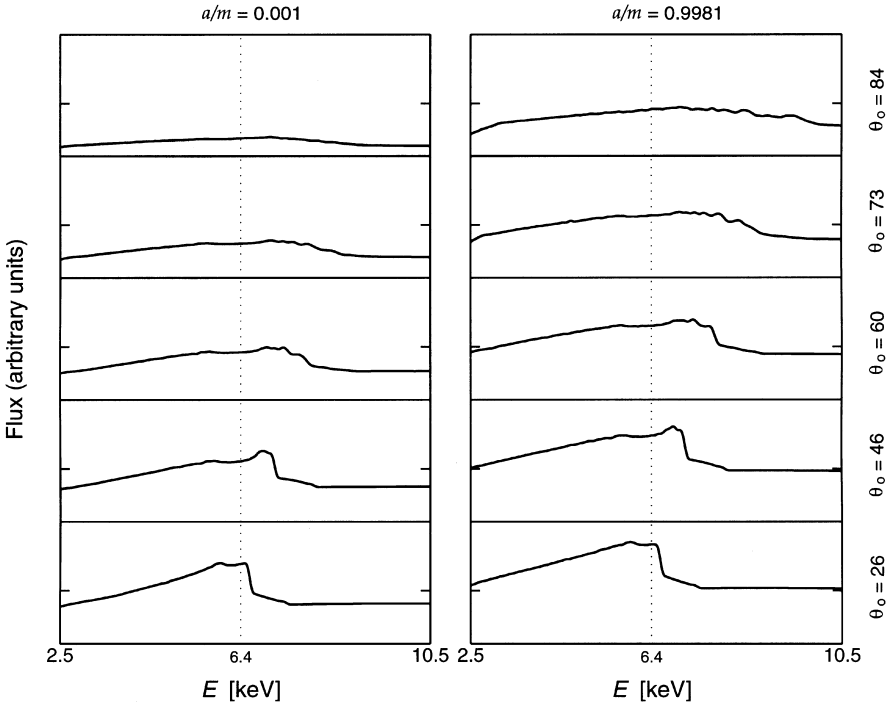

Figure 7. As in previous figure but for $h = 10\,m$.

the underlying continuum. Thus the spectral features are spread across a broad range of energies and may become difficult to observe. Similar behaviour could be obtained for static black holes if efficient emission were allowed from inside the innermost stable orbit, but Young et al. (1998) noticed that in this case a large absorption edge beyond 6.9 keV should appear, and this is usually not observed in AGN.

2.4 The line profile

The qualitative behaviour of the observed line profiles as a function of observer's inclination is very intuitive. When a disc is observed almost pole-on, the iron line gets somewhat broadened and redshifted because of the deep potential well and transverse Doppler effect owing to the rapid orbital motion of the matter.

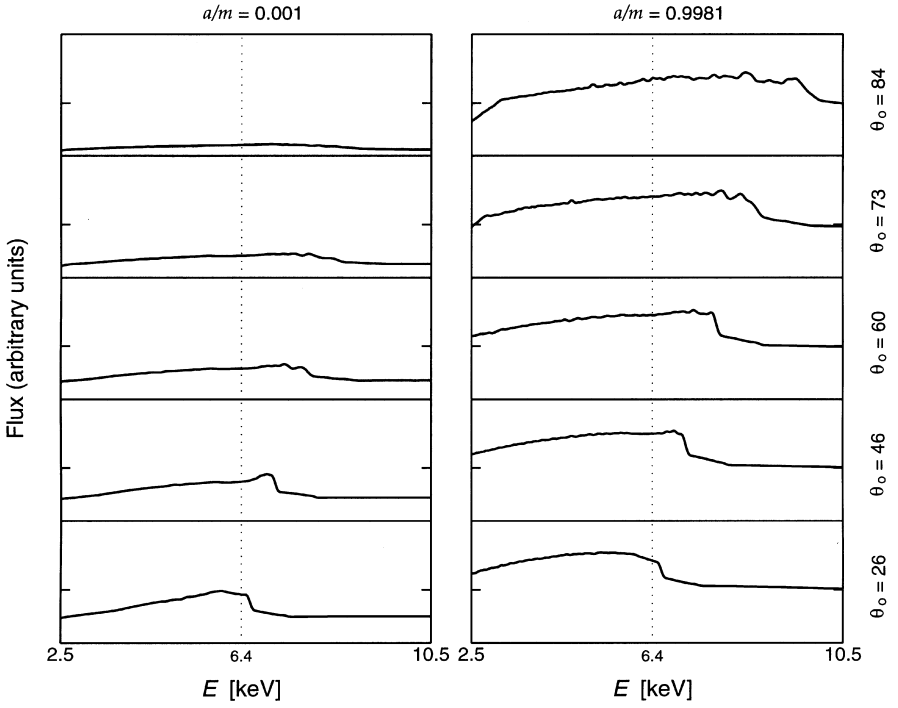

Figure 8. As in previous figure but for $h = 6\,m$.

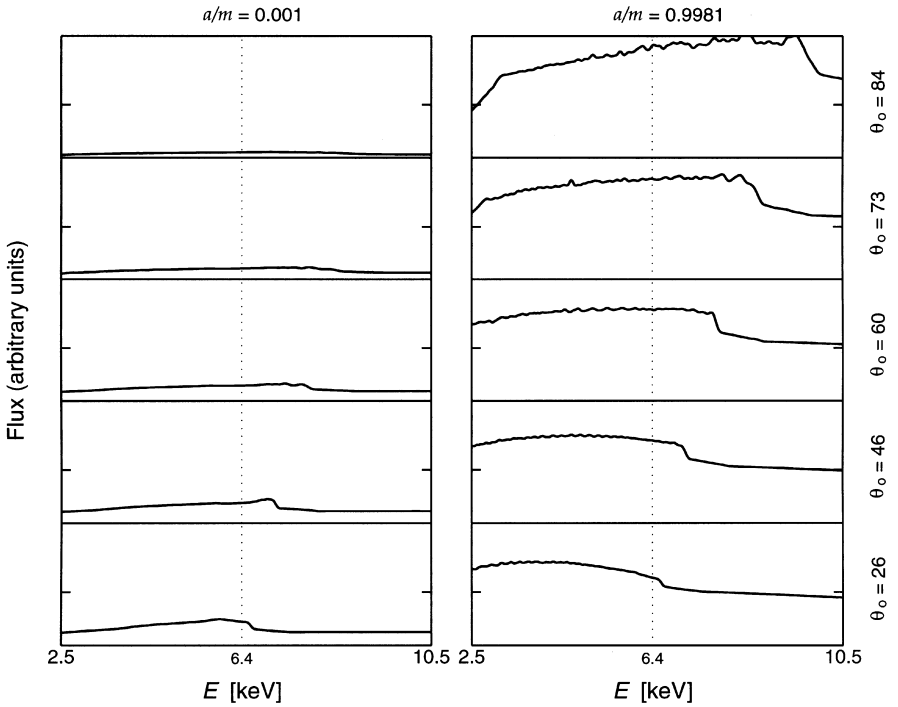

Figure 9. As in previous figure but for $h = 4\,m$.

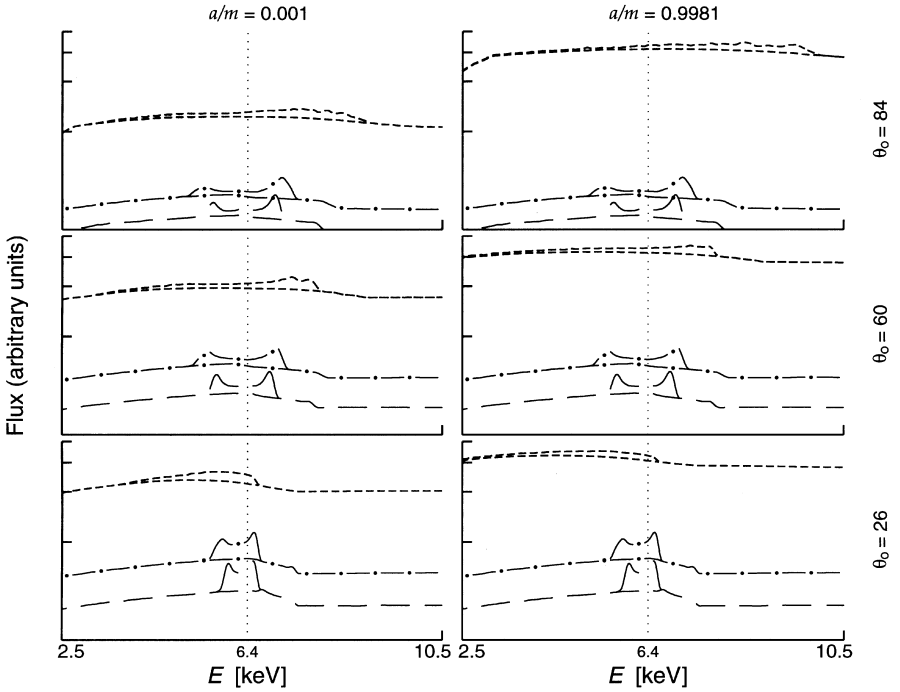

Figure 10. Contributions to the total profile for $h = 6\,m$ from three subsections of the disc are shown in this figure: r/m extending from $r_{\rm ms}$ up to 34 (short-dashed), 34–67 (dash-dotted) and 67–100 (long-dashed). The underlying curves of the reflection continuum are also plotted. Three values of inclinations (corresponding to $\cos\theta_{\rm o} = 0.1$, 0.5 and 0.9) are considered. The vertical scale is logarithmic.

This effect is more pronounced in the extreme Kerr case, when the emitting material, still on stable orbits, extends down almost to the very horizon. The broadening of the observed spectral features is particularly evident when strongly anisotropic emissivity laws, resulting from small h, are considered. As the disc inclination increases, the iron line becomes substantially broader, with the well-known double-peaked profile resulting from the Doppler shift of the radiation coming from opposite sides of the disc. The interplay of Doppler effects and gravitational light bending determines the details of the profile. The relative distance of the two horns increases with the inclination angle; then the horns and the iron edge almost disappear as individual and well recognizable features for very high inclinations when the Doppler effect is maximum (disc observed edge-on). Therefore, such horns are well visible only at intermediate inclinations. In this situation the blue peak is substantially higher than the red one, as a result of Doppler boosting. A quantitative account of all these effects requires one to adopt specific models and to calculate profiles numerically.

Figures 5–10 show the line profiles corresponding to different h in our model. It is evident that the effects of the anisotropic illumination can be enormous, causing a substantial amount of the re-emitted flux to be highly redshifted, especially in the low-h case. When the source is very close to the black hole, because of strong anisotropy, only the innermost part of the disc contributes to the line and to the reflection continuum fluxes. As a consequence, spectral features can be huge in the Kerr metric, whereas in the Schwarzschild case they gradually disappear if no efficient re-emission is possible from $r < 6\,m$.

The adopted emissivity law is clearly a key ingredient in the calculations of reflected spectra. Flat local emissivity laws apply when the source is distant from the hole ($h \gg r_{\rm g}$), and result in spectra which show very weak dependence on the black hole angular momentum. On the other hand, with steep emissivities (low h) the observed spectra strongly depend on a/m.

The detailed line profiles contain a wealth of information which can in principle be compared with observed data, but it may be useful to describe them also by integral quantities which also can be determined from data with lower resolution. In the next section we will consider the line equivalent width (EW), the centroid energy ($E_{\rm cen}$) and the geometrical width (σ). Here, EW is defined in terms of radiation fluxes (line and continuum) as $\mathrm{EW} = \int F_{\rm line}(E)\,\mathrm{d}E/F_{\rm cont}(E = E_{\rm line})$, where the underlying continuum can be either the direct, or the reflected one, or their sum; i.e. $F_{\rm cont} = F_{\rm dir} + F_{\rm ref}$. $E_{\rm line}$ is the rest energy of the line, i.e. 6.4 keV for the iron Kα line.

3 COMBINED EFFECTS AND INTEGRAL QUANTITIES

When dealing with low energy resolution detectors and/or faint sources, a detailed study of the line profile may not be possible. In these cases, one can resort to integral quantities. In Figs 11–13 we present the equivalent widths of the iron Kα fluorescent line for different cases. As a check, we verified that in the Schwarzschild case the results were in agreement with those of Matt et al. (1992).

We carried out calculations for several different values of the model parameters h, a, $\theta_{\rm o}$ and for different sizes of the disc. Apart from the above mentioned strong h dependencies of the observed spectra, it turns out that the radial extension of the disc is an important parameter determining the reflection continuum and affecting EWs.

In Fig. 11, the height of the source is fixed to $20\,m$. The upper three curves correspond to an outer radius $r_{\rm out} = 1000\,m$, while those below to $r_{\rm out} = 100\,m$. For both sets, the curves refer to (from top to bottom): (i) $r > r_{\rm in} = 1.23\,m$ (the innermost stable orbit in the Kerr metric, given the fiducial value of $a/m = 0.9981$, Thorne 1974); (ii) $r > r_{\rm in} = 6\,m$ (the innermost stable orbit in the

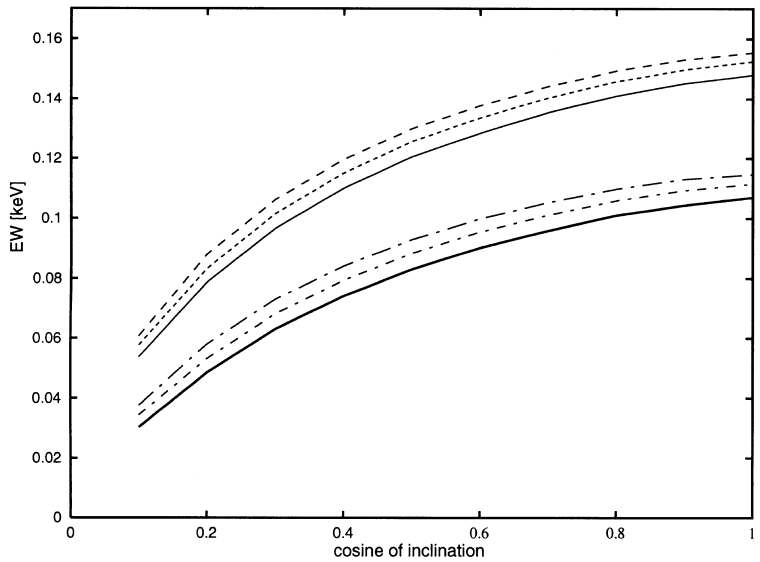

Figure 11. Equivalent width as a function of the cosine of inclination. Here, $h = 20\,m$, $a/m = 0.9981$. For such a large value of h, even with the almost extreme value of a/m, the results are very similar to the non-rotating case and thus agree well with the values in Matt et al. (1992). Here EWs refer to the direct continuum only and the solid angle distortion is negligible ($f \sim 1$). See the text for more details.

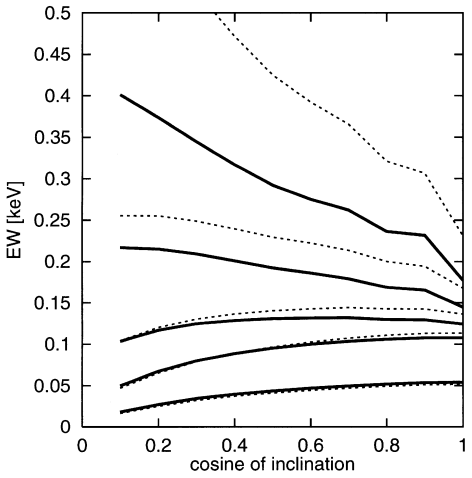

Figure 12. Equivalent width versus cosine of the observer's inclination angle, for different illuminations and a disc extending from the innermost stable orbit up to $100\,m$. The solid lines refer to EWs with respect to the total underlying continuum and the dashed ones to EWs with respect to the direct contribution only. From top to bottom, the curves are for a source located at $h/m = 4$, 6, 10, 20 and 100, respectively. The black hole spin parameter is $a/m = 0.9981$.

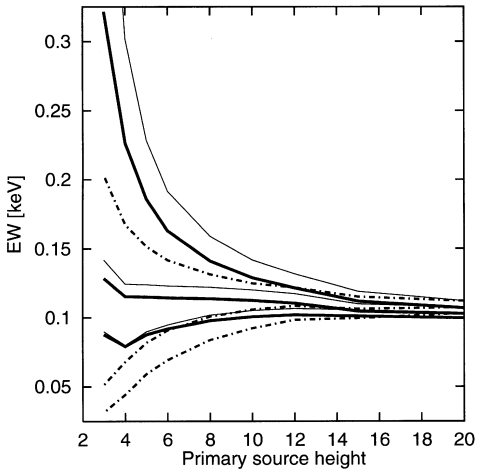

Figure 13. EW dependence on the source height h, for an observer inclination fixed at 30° and a disc extending from the innermost stable orbit up to $100\,m$. Three values have been considered for the black hole spin (from top to bottom): $a = 0.9981\,m$, $0.5\,m$ and $0.001\,m$. See the text for more details.

Schwarzschild metric): we found that the resulting values for static and for rotating holes are very similar in this case; (iii) $r > r_{\rm in} = 10\,m$: values for static and for rotating black holes are almost identical.

In the other figures the strong dependence on the source parameter h is evident. In our calculations we also accounted for the effect of the light-rays distortion on the primary flux, i.e. for the fact that the solid angle Ω of the direct continuum, which escapes to infinity (arriving directly from the primary source to the observer), diminishes considerably when the source is near the black hole (low h). The effect is accounted for by introducing an h-dependent factor $f(h) = \Omega_{\rm inf}/\Omega_{\rm inf,cl}$ which multiplies $F_{\rm dir}$ in the definition of EW. As expected, f approaches unity if the source is far away from the hole.

Fig. 12 shows the equivalent width as a function of the cosine of inclination, $\mu = \cos\theta_{\rm o}$. The slope of EW(μ) becomes inverted around $h \sim 10\,m$: for larger values of h we obtain EW *decreasing* with μ, as in the Schwarzschild case, whereas for $h \lesssim 10\,m$ EW *increases* when μ decreases. This is a direct consequence of both the large efficiency of line emission and the enhanced influence of light bending from the innermost Kerr orbits, which strongly affects the profiles. This behaviour is less pronounced when EWs with respect to the total continuum (direct plus reflected; cf. solid lines) are considered, the reason being that the Compton-reflected contribution, $F_{\rm ref}$, increases together with the line contribution,

Table 1. Table of integral quantities characterizing the iron Kα line profiles: centroid energy and geometrical width (in eV) and equivalent width (in keV). Comparison is given between corresponding quantities for a fast rotating and a non-rotating (in parenthesis) black hole.

$\cos\theta_o$		$h=4\,m$		$h=6\,m$		$h=10\,m$		$h=20\,m$		$h=100\,m$	
	E_{cen}	7.65	(6.77)	7.45	(6.73)	7.18	(6.64)	6.78	(6.52)	6.44	(6.44)
0.1	σ	1.71	(1.29)	1.71	(1.27)	1.62	(1.17)	1.31	(0.96)	0.64	(0.61)
	EW	401	(30)	217	(35)	103	(38)	50	(36)	18	(18)
	E_{cen}	6.50	(6.65)	6.56	(6.63)	6.56	(6.57)	6.49	(6.47)	6.38	(6.38)
0.3	σ	1.63	(1.26)	1.56	(1.23)	1.38	(1.14)	1.07	(0.96)	0.64	(0.62)
	EW	345	(58)	209	(66)	125	(72)	80	(68)	34	(34)
	E_{cen}	5.71	(6.36)	5.97	(6.36)	6.17	(6.35)	6.29	(6.34)	6.34	(6.34)
0.5	σ	1.50	(1.13)	1.42	(1.10)	1.23	(1.02)	0.95	(0.86)	0.58	(0.57)
	EW	292	(72)	192	(82)	131	(89)	95	(85)	44	(43)
	E_{cen}	5.08	(6.01)	5.47	(6.03)	5.82	(6.08)	6.09	(6.17)	6.27	(6.27)
0.7	σ	1.35	(0.93)	1.26	(0.91)	1.08	(0.84)	0.82	(0.71)	0.48	(0.47)
	EW	262	(77)	179	(88)	132	(97)	103	(95)	49	(49)
	E_{cen}	4.53	(5.64)	5.01	(5.68)	5.49	(5.79)	5.88	(5.97)	6.19	(6.19)
0.9	σ	1.20	(0.67)	1.11	(0.65)	0.92	(0.61)	0.66	(0.51)	0.33	(0.31)
	EW	232	(79)	165	(91)	130	(101)	107	(100)	53	(53)

F_{line}, when the primary source height decreases, and eventually dominates.

In Fig. 13, EWs versus three different definitions of the continuum are shown for the sake of illustration: thick solid lines refer to EWs with respect to the total underlying continuum, taking into account the solid angle distortion owing to the space–time curvature; thin solid lines have been computed in a similar manner, but with respect to the direct continuum only; finally, the dash-dotted lines have been plotted with respect to the direct continuum only, and they do not include the solid angle distortion effect. It is worth noticing that, owing to efficient emission from the innermost region, in the extreme Kerr case one obtains EW values very much enhanced at low h's.

Table 1 reports integral quantities (centroid energy, line width, and equivalent width with respect to the total continuum) of the line profiles for selected values of the parameters h and θ_o. The table refers to a disc extending up to 100 gravitational radii and a maximally spinning black hole; values for a static hole (with $r_{in}=6\,m$) are given in parentheses for comparison. In Table 1, E_{cen} and σ are expressed in keV while EW is in eV.

Finally, a word of caution is needed here on the effect of the iron abundance. The EW strongly depends on abundance (e.g. Matt, Fabian & Reynolds 1997) but fortunately the other integral parameters of the line do not depend on abundance as much. Moreover, the reflection component depends on the iron abundance in an easily recognizable way, i.e. changing the depth of the iron edge (Reynolds, Fabian & Inoue 1995). Strong constraints have been derived in the case of MCG–6-30-15 (Lee et al. 1999). Therefore one can hope to separate the influence of poorly known iron abundances from other effects.

4 CONCLUSIONS

We calculated the relativistic effects on both the iron line and the reflection continuum emitted in the innermost regions of accretion discs around spinning black holes in AGN and BHCs. The calculations are fully relativistic with respect both to the primary emission (illumination from a central source) and to the secondary one (disc reflection), so that the line profiles are in this sense computed self-consistently.

We found that the adopted geometry of the source copes very well with the observed widths and energy centroids of the spectral features around 6.4 keV. However, the final assessment of one of the few viable models requires more detailed comparisons than it has been possible to do so far with the currently available data. Predicted values should be compared against high-resolution data, together with the results of alternative scenarios, such as quasi-spherical accretion and further line broadening owing to Comptonization.

The development of a XSPEC compatible code, making use of a big atlas of geodesics, is in progress. This will enable a fast fitting of the data.

The results presented here are thus relevant for the near future high-sensitivity X-ray observatories, like *XMM*, as far as the iron line is concerned. We have to wait for missions like *Constellation-X*, with its very large sensitivity and broad-band coverage, in order to simultaneously examine both the iron line and the reflection continuum in the desired detail.

ACKNOWLEDGMENTS

VK acknowledges support from the grants GACR 205/00/1685 and 202/99/0261 in Prague.

REFERENCES

Bao G., Wiita P. J., Hadrava P., 1998, ApJ, 504, 58
Bardeen J. M., Press W. H., Teukolsky S. A., 1972, ApJ, 178, 347
Bromley B. C., Chen K., Miller W. A., 1997, ApJ, 475, 57
Chandrasekhar S., 1983, The Mathematical Theory of Black Holes. Clarendon Press, Oxford
Cunningham C. T., 1975, ApJ, 202, 788
Cunningham C. T., Bardeen J. M., 1973, ApJ, 183, 273
Čadež A., Fanton C., Calvani M., 1998, New Astron., 3, 647
Čadež A., Calvani M., Di Giacomo C., Marziani P., 1999, New Astron., submitted
Dabrowski Y., Fabian A. C., Iwasawa K., Lasenby A. N., Reynolds C. S., 1997, MNRAS, 288, L11
Fabian A. C., Rees M. J., Stella L., White N. E., 1989, MNRAS, 238, 729
Fanton C., Calvani M., de Felice F., Čadež A., 1997, PASJ, 49, 159
Guilbert P. W., Rees M. J., 1988, MNRAS, 233, 475
Hameury J.-M., Marck J.-A., Pelat D., 1994, A&A, 287, 795
Henry G., Petrucci P. O., 1997, A&A, 326, 87
Iwasawa K. et al., 1996, MNRAS, 282, 1038
Karas V., Vokrouhlický D., Polnarev A., 1992, MNRAS, 259, 569
Karas V., Lanza A., Vokrouhlický D., 1995, ApJ, 440, 108
Kojima Y., 1991, MNRAS, 250, 629

Laor A., 1991, ApJ, 376, 90
Lee J. C., Fabian A. C., Brandt W. N., Reynolds C. S., Iwasawa K., 1999, MNRAS, 310, 973
Lightman A. P., White N. E., 1988, ApJ, 335, 57
Maciołek-Niedźwiecki A., Magdziarz P., 1998, in Chakrabarti S. K., ed., Observational Evidence for Black Holes in the Universe. Kluwer, Dordrecht (astro-ph/9805328)
Mannucci F., Salvati M., Stanga R. M., 1992, ApJ, 394, 98
Martocchia A., Matt G., 1996, MNRAS, 282, L53
Martocchia A., Matt G., 1997, Proc. 12th Italian Conference on General Relativity and Gravitational Physics. World Scientific Publ., Singapore
Matt G., Perola G. C., Piro L., 1991, A&A, 247, 25
Matt G., Perola G. C., Piro L., Stella L., 1992, A&A, 257, 63 (Erratum in A&A, 263, 458)
Matt G., Fabian A. C., Reynolds C. S., 1997, MNRAS, 289, 175
Nandra K., George I. M., Mushotzky R. F., Turner T. J., Yaqoob T., 1997, ApJ, 477, 602
Page D. N., Thorne K. S., 1974, ApJ, 499, 191
Reynolds C. S., Begelman M. C., 1997, ApJ, 488, 109
Reynolds C. S., Fabian A. C., Inoue H., 1995, MNRAS, 276, 1311
Reynolds C. S., Young A. J., Begelman M. C., Fabian A. C., 1999, ApJ, 514, 164
Tanaka Y. et al., 1995, Nat, 375, 659
Thorne K. S., 1974, ApJ, 191, 507
Young A. J., Ross R. R., Fabian A. C., 1998, MNRAS, 300, L11
Yu Q., Lu Y., 2000, MNRAS, 311, 161
Życki P. T., Done C., Smith D. A., 1997, ApJ, 488, L113
Życki P. T., Done C., Smith D. A., 1998, ApJ, 496, L25

APPENDIX: FITTING FORMULAE FOR THE EMISSIVITY LAWS AND INTEGRAL QUANTITIES

Local emissivities of the disc surface have been plotted in Fig. 2. In Table A1 we provide a practical fit of the emissivities, which can be useful in calculations. We used a simple law of the type:

$$\epsilon(r) = c_1 r^{-\lambda_1} + c_2 r^{-\lambda_2}. \quad (1)$$

The adoption of function (1) for the fitting enables comparisons with the power laws, which are commonly used in standard line-profile calculations. Attempts to derive the emissivity dependence from radius by 'inverting' observed line profiles have also been made, e.g. by Čadež et al. (1999), Dabrowski et al. (1997) and Mannucci, Salvati & Stanga (1992).

In Table A2 we provide coefficients of the least-squares fitting for the observable quantities: $E_{\rm cen}(h)$, $\sigma(h)$, and EW(h). Here we used quadratic polynomials of the form

$$a_0 + a_1\, h/m + a_2\, (h/m)^2, \quad (2)$$

which can approximate h dependences in the range $4m \le h \le 20\,m$ with sufficient accuracy. For the whole interval, up to $h = 100\,m$, we used more precise spline fits; the corresponding MATLAB script is available from the authors (this can be used for the numerical inversion to obtain parameters of the model, i.e. a/m, $\theta_{\rm o}$ and h/m, in terms of the three observables).

This paper has been typeset from a TEX/LATEX file prepared by the author.

Table A1. Results of fitting the emissivity laws for different source heights (see the Appendix for detailed explanation). All coefficients have been obtained for a maximally rotating hole, except for the row $h_{\rm cl} = 5\,m$, which refers to the purely classical (i.e. Euclidean) case with the rays not distorted by gravitation. For $r > 6\,m$ (which is the case for stable orbits in the Schwarzschild metric) the emissivity is only weakly affected by the black hole spin, while the effect of rotation is substantial for small values of h.

	c_1	λ_1	c_2	λ_2
$h = 2\,m$	0.02268	38.38706	0.000122	6.14786
$h = 3\,m$	0.00146	24.47516	0.000059	0.00006
$h = 4\,m$	0.00324	30.85495	0.000039	4.70109
$h = 5\,m$	0.00640	35.36543	0.000025	4.49187
$h = 6\,m$	0.00968	34.27642	0.000013	3.75576
$h = 8\,m$	0.27139×10^{-4}	8.74175	0.01662×10^{-4}	1.74206
$h = 10\,m$	0.99815×10^{-5}	6.05660	0.04793×10^{-5}	1.14952
$h = 12\,m$	0.42940×10^{-5}	4.42939	0.01590×10^{-5}	0.81154
$h = 15\,m$	0.27182×10^{-5}	4.64923	0.01451×10^{-5}	0.89655
$h = 20\,m$	0.98182×10^{-6}	3.66965	0.05796×10^{-6}	0.72744
$h = 100\,m$	0.59002×10^{-5}	1.05533	-0.59023×10^{-5}	1.05622
$h_{\rm cl} = 5\,m$	0.10084×10^{-4}	0.29168	-0.09948×10^{-4}	0.28796

Table A2. Coefficients of the least-squares polynomial fits to h dependences of $E_{\rm cen}$, σ and EW, as predicted in our model. The angular-momentum parameter is $a = 0.9981\,m$; for comparison, the values resulting from computations with the Schwarzschild metric are given in parentheses.

$\cos\theta_{\rm o}$		a_2		a_1		a_0	
0.1	$E_{\rm cen}$	0.00243	(0.000594)	−0.112	(−0.0301)	8.05	(6.88)
	σ	−0.00103	(-8.77×10^{-5})	−0.000877	(−0.019)	1.74	(1.37)
	EW	2.85	(−0.0979)	−88.8	(2.68)	687	(21.4)
0.3	$E_{\rm cen}$	−0.0011	(0.000198)	0.0251	(−0.0162)	6.43	(6.71)
	σ	0.000643	(0.000111)	−0.0509	(−0.0217)	1.83	(1.35)
	EW	2.07	(−0.173)	−65.1	(4.74)	555	(42.6)
0.5	$E_{\rm cen}$	−0.00414	(3.69×10^{-5})	0.134	(−0.00223)	5.27	(6.37)
	σ	0.00104	(0.000136)	−0.0598	(−0.0203)	1.73	(1.21)
	EW	1.5	(−0.206)	−47.4	(5.68)	445	(53.6)
0.7	$E_{\rm cen}$	−0.00614	(−0.000161)	0.208	(0.014)	4.38	(5.95)
	σ	0.00118	(0.000111)	−0.0616	(−0.0167)	1.58	(0.999)
	EW	1.21	(−0.224)	−38.3	(6.44)	384	(55.8)
0.9	$E_{\rm cen}$	−0.00769	(−0.00042)	0.266	(0.031)	3.62	(5.52)
	σ	0.00127	(1.34×10^{-19})	−0.0647	(−0.01)	1.44	(0.71)
	EW	0.952	(−0.239)	−30	(6.98)	327	(56)